Numerical Investigation of the Effects of Sand Collision on the Aerodynamic Behaviour of a High-Speed Train Subjected to Yaw Angles

J. Wang[1, 2, 3], D. Liu[1, 2, 3], G. Gao[1, 2, 3], Y. Zhang[1, 2, 3] and J. Zhang[1, 2, 3†]

[1] *Key Laboratory of Traffic Safety on Track of Ministry of Education, School of Traffic & Transportation Engineering, Central South University, Changsha 410075, China*

[2] *Joint International Research Laboratory of Key Technology for Rail Traffic Safety, Central South University, Changsha 410075, China*

[3] *National & Local Joint Engineering Research Center of Safety Technology for Rail Vehicle, Changsha 410075, China*

[†]*Corresponding Author Email: jie_csu@csu.edu.cn*

ABSTRACT

In this paper, the aerodynamic performance of the head car of a CRH2 train running in sandstorms was investigated. A numerical simulation method based on Realizable *k-ε* turbulence model was used to explore the flow features around the high-speed train. The accuracy of mesh resolution and methodology of CFD was validated by wind tunnel tests. A discrete phase model (DPM) was adopted to investigate the effects of sand particle properties (diameter and restitution coefficient) on the aerodynamic performance of the head car. Yaw angle effects with the sand-laden flow on the aerodynamic coefficient were also discussed. The results show that the drag force, lift force, lateral force, and overturning moment of the head car increase significantly due to the sand, and the sand particle properties have dominant effects on the aerodynamic performance of the head car. The impact probability of sand particles on the vehicle increases with the sand particle diameter and the yaw angle increasing. Larger restitution coefficients lead to lager forces of the head car, resulting in more contribution to the aerodynamic coefficients. Owing to the sand collision, a larger yaw angle causes more contribution to the aerodynamic performance of the head car, and the influence of sand properties on the drag force, lateral force and overturning moment are enhanced with the increase of the yaw angle. Using appropriate coatings around the high-speed train can not only reduce the energy consumption, but also improve the lateral stability and the critical operational speed of the high-speed train in the sandstorms.

Keywords: High-speed train; Aerodynamic performance; Sand impact; Discrete phase model; Numerical simulation.

NOMENCLATURE

b	lateral reference length of the vehicle	M_x	overturning moment of the vehicle
C	lateral force of the vehicle	n	size of the first cell in the normal direction
C_C	lateral force coefficient	Re_p	relative Reynolds number
C_d	drag coefficient of sand particles	S	reference area of the vehicle
C_D	drag coefficient	S_{tk}	Stokes number
C_L	lift coefficient	U_{ref}	uniform wind speed given at inlet
C_p	static pressure coefficient	U	normalized velocity of air
D	drag of the vehicle	U^*	friction velocity
d_p	diameter of sand particles	u	velocity of air
F_{mean}	mean force exerting on the train due to sand	u_p	velocity of sand particles
g	gravity acceleration		
H	height of the vehicle	μ	dynamic viscosity of air
k	turbulent kinetic energy	ρ_p	density of sand particles
L	lift of the vehicle	ρ	density of air
m_p	mass of sand particles	v	kinematic viscosity of air

ε	dissipation rate
β_w	yaw angle

Δl_i distance between successive particles

1. INTRODUCTION

When running under strong crosswind conditions, especially at exposed locations, such as, the bridges or embankments, the high-speed train would suffer abruptly increasing aerodynamic forces and moments which reduce its stability (Baker 1991a). Sometimes, the high-speed train runs in some extreme climates, such as strong crosswinds and sandstorms, the running safety of the high-speed train can be affected significantly (Baker 1991b). Moreover, the operational safety may be highly threatened by the increase of train speed, which even leads to derailment, overturning or other severe train accidents (Orellano 2009). For instance, serious overturning accidents have reported on the Xinjiang railways in the strong windy desert areas, as shown in Fig. 1. Thus, the aerodynamic performance and operational safety of the high-speed trains under strong winds with sand are important issues to study.
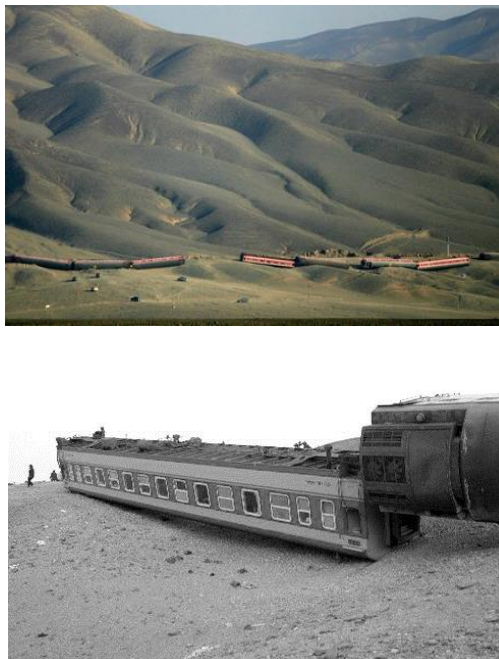

Fig. 1. Train accident on the Xinjiang railway due to strong sandstorms.

To improve the crosswind stability of high-speed trains, numerous studies have been done mainly using two approaches: wind tunnel tests and numerical simulations (Giappino *et al.* 2016). Several wind tunnel tests have been conducted to study the running stability of high-speed trains under crosswinds (Gilbert *et al.* 2013, Tomasini *et al.* 2014, Dorigatti *et al.* 2015, Cheli *et al.* 2013, Bocciolone *et al.* 2003). Besides of those wind tunnel tests, numerical simulations also have been carried out to study these issues (Cheli *et al.* 2006, Hemida and Krajnović 2010, Hemida *et al.* 2014, Cheli *et al.* 2010, Diedrichs 2008, Zhang *et al.*

2015, Zhang *et al.* 2017). However, the studies mentioned above are paid less attention to the effect of sandstorms, and how the sand affects the aerodynamic characteristics and running safety of the trains are unclear. The ambient wind and train induced airflow blow the sand along the railway line, and the sand particles impact on the train surface with such a high speed, which has great effects on the operational safety.

In this paper, a two-phase gas-solid method was used to simulate this phenomenon. Currently, for this kind of sand-wind flow, two approaches, i.e. Eulerian-Eulerian (E-E) and Eulerian-Lagrangian (E-L), are usually adopted (Balachandar and John 2010). In the E-E, both of air and sand phases are treated to be continuous. However, in this particular strong sandstorm case, the volume fraction of the sand is just about $1.08e^{-7}$ (Xiong *et al.* 2011), so it is unreasonable to treat the sand as a continuous phase. Meanwhile, the E-L requires the discrete volume fraction to be less than 10%. For this purpose, the E-L is considered to be more appropriate. In the E-L, the air is treated as a continuous phase by solving the N-S equations, while the sand particles are treated as a discrete phase are tracked individually in order to obtain their trajectories. Additionally, the E-L has been successfully used to study the two-phase gas-solid flow in wide industrial applications (Nieto 2010, Barisam and Shams 2015, Safikhani and Mehrabian 2016). Moreover, Paz *et al.* (2015) investigated the aerodynamic performance of high-speed trains in sandstorms using E-L approach. In their study, only the sand particles impacting on the windward surface of leading vehicle at the yaw angle of 0 degree was considered while it is hard to occur as the high-speed trains run in the wind-sand area. This paper simulated the aerodynamic performance of high-speed train encountering the crosswind and sand collision, which better meets the requirement of engineering application.

In this paper, the E-L approach was used to simulate the motion of the sand particles around the train under strong crosswind and sandstorm conditions. The aim of this paper is to investigate the aerodynamic performance of the high-speed train in the sand-laden flow, to know how the sand particles affect the aerodynamic coefficients (drag coefficient, lateral force coefficient, lift force coefficient and overturning moment coefficient) of the head car, and to study how the sand properties (attacked angle, particle diameter and restitution coefficient between the sand particles and train surface) influence the aerodynamic performance of the head car.

This paper is organized as follows. In Section 2, the mathematical model, selected geometric model, computational grid, boundary conditions and the parameters setting for the particle tracking are given together. In Section 3, the numerical results of the

single continuous air phase are compared with the wind tunnel tests to validate the accuracy of the resolution of the mesh and methodology. The aerodynamic coefficients of the head car in each case are compared and analysed, and how the sand particles influence the aerodynamic performance is also explained. Finally, the conclusions are drawn in Section 4.

2. CFD ANALYSIS

2.1 Mathematical Model

Based on Reynolds-averaged motion equations, the Realizable k - ε turbulence model with wall function treatment was selected to simulate the continuous phase (air flow fields). The Reynolds average method which not only ensures the accuracy of calculation, but also saves the computing resources, has been widely used in engineering. The details of the continuity equation, momentum equation and related parameters are discussed by John and Anderson (1995). The details of k equation and ε equation are given by Shih and Liou (1995). To simulate the discrete phase (sand particles), the DPM model implemented in Fluent was used. The movement parameter (acceleration, velocity and displacement etc.) can be obtained by integrating the differential equations that describe the forces acting on the sand particles. And the differential equations are presented as follows (Spalding 1981, Guan and Tu 2010, Ni and Li 2006).

$$\frac{du_p}{dt} = \frac{18\mu}{\rho_p d_p^2} \frac{C_d \, \mathrm{Re_p}}{24} \left(u - u_p \right) + \frac{g(\rho_p - \rho)}{\rho_p} \qquad (1)$$

where u is the velocity of the continuous phase; u_p is the velocity of sand particles; μ is the dynamic viscosity of air; d_p is the diameter of sand particles; ρ_p is the density of sand particles; ρ is the density of the continuous phase; g is the gravity acceleration; C_D, the drag coefficient of the sand particle, is defined as:

$$C_d = \alpha_1 + \frac{\alpha_2}{\mathrm{Re}} + \frac{\alpha_3}{\mathrm{Re}^2} \qquad (2)$$

where α_1, α_2, and α_3 are constants that apply over several ranges of Re given by Morsi and Alexander (1972). Here, the relative Reynolds number is defines as:

$$\mathrm{Re_p} = \frac{\rho d_p \left| u_p - u \right|}{\mu} \qquad (3)$$

2.2 Geometry Model and Computational Domain

Although the DPM can offer a more comprehensive description of the particle movement, it also requires more computing resources (Zhang and Chen 2007). Thus, only the aerodynamic performance of the head car was studied in this paper. Since the sand particles are failure to comply with the similar criteria so that a full-scale simplified CRH2 train without the pantographs was adopted in this paper. And the computational model

consists of the head car and 1/3 length of the second car in order to get the correct boundary conditions of the head car (Cheli *et al*. 2010), as shown in Fig. 2. To simulate the air flow field around the train accurately, the single-track ballast and rail (STBR) scenario was adopted in this study.

In this paper, five yaw angles, i.e. 0, 5.15, 10.22, 15.14 and 19.73 degrees, were considered, as defined in Fig, 3(a). Here the domain keeps the same, but the train model with the ballast is rotated to the specified angle (Cheli *et al.* 2010). The rotation axis is in the middle of the head car. Figure 3(b) presents the domain without the yaw angle. The distance of the train nose from the inlet is 8*H*, while the rear to the pressure outlet is 30*H*. The height and the width of the computational domain are 10*H* and 20*H*, respectively (Hemida *et al.* 2014).
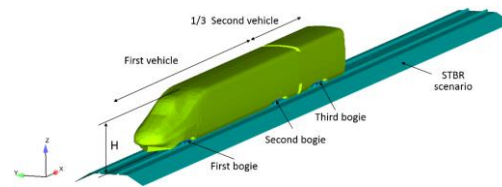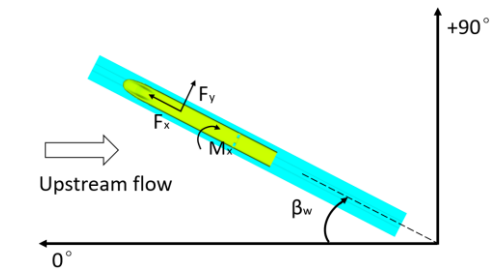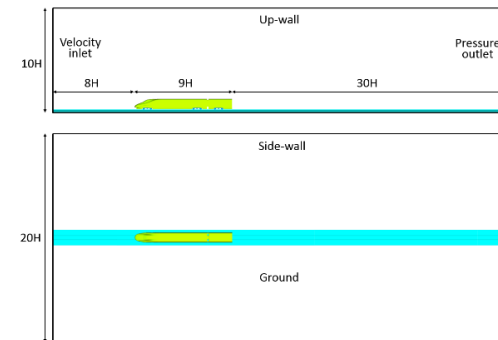

Fig. 2. Geometric model.

(a)

(b)

Fig. 3. Computational domain: (a) Reference system adopted for the aerodynamic performance and for the yaw angles and (b) Computational domain at the yaw angle of 0 degree.

2.3 Computational Mesh and Boundary Conditions

The OpenFOAM mesh generator package was applied to build the hexahedral dominant mesh around the train and bogie, as shown in Fig. 4. The

refining meshes were applied to the near region around the train and bogie. In addition, a uniform transition mode with a constant growth factor between the fine grid and the sparse grid was adopted, which not only ensures the requirements of accuracy, but also saves the computing resources. The quality of meshes was verified to ensure the maximum skewness of each cell was below 4.0. Where, the skewness is defined as the distance from the face centre to the intersection of the line between the two adjacent cell centres which is then normalised by the centroid-to-centroid distance of the adjacent cell (Flynn *et al.* 2016). Ten prism layers in boundary layers were applied to the train and bogie surface in order to catch the flow characteristics in the boundary, and the boundary layer configuration can be seen in Fig. 4(b). The thickness of the first boundary layer is 0.42mm, and the y^+ (the non-dimensional distance to the wall), over the high-speed train's surface is between 30 and 60, which ensures the use of wall function in the Realizable k-ε turbulence model. The y^+ is defined as $y^+{=}nU^*/v$, where U^* is the friction velocity, n is the distance between the first node and the train surface in the wall normal direction and v is the kinematic viscosity. Mesh sensitivity testing was also conducted to determine whether the numerical results are a function of mesh density. Since the overturning moment is totally determined by the lift and lateral forces, so the grid sensitivity test was only conducted to check the drag coefficient, lift coefficient and lateral force coefficient. According to the CEN European Standard (CEN European Standard 2013), the normalized aerodynamic coefficients are defined as follows:

$$C_D = D / (0.5\rho U_{ref}^2 S) \tag{4}$$

$$C_L = L / (0.5\rho U_{ref}^2 S) \tag{5}$$

$$C_S = C / (0.5\rho U_{ref}^2 S) \tag{6}$$

$$C_{Mx} = M_x / (0.5\rho U_{ref}^2 Sb) \tag{7}$$

where, S is the reference area that is projected on the cross-section of the train, is 11.2m²; D, L, C and M_x are the drag, lift, lateral force and overturning moment calculated with respect to the lee rail, respectively; C_D, C_L, C_C and C_{Mx} are the drag, lift, lateral force and overturning moment coefficients, respectively; U_{ref} is the uniform wind speed given at the velocity inlet. b is the lateral reference length which is 0.574m.

On the basis of the same value of y^+, different meshes with different spatial resolutions along the directions of x and y axes were compared (i.e., Coarse, Baseline and Fine grids). Relative to the Baseline grid, the Coarse grid was reduced by a factor of $\sqrt{2}$ in the number of grid point in both x and y directions and the Fine grid was generated by increasing the refinement in each (x and y) direction by a factor of two (Zhu *et al.* 2015). The numbers of volume cells in the Coarse, Baseline and Fine cases are approximately 12 million, 24 million and 96 million, respectively. The numerical results of

aerodynamic coefficients of the head car at the yaw angle of 10.22 degrees on the Coarse, Baseline and Fine meshes are presented in Table 1. For the Baseline mesh, the differences of the drag coefficient, lift coefficient and lateral force coefficient on are within 2.3%, 2.1% and 2.5%, respectively, as compared to the Fine mesh, which indicates that the Baseline grid has an adequate resolution. The results on the Coarse mesh present large differences, meaning this coarse mesh should be not used in the next investigation. Therefore, the Baseline grid is utilized for the further study.
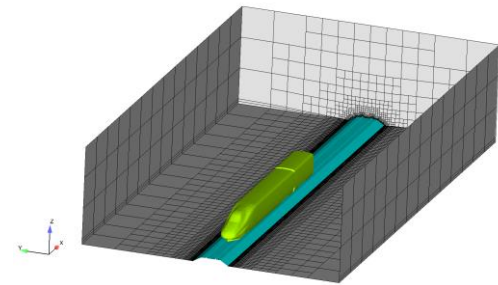
(a)
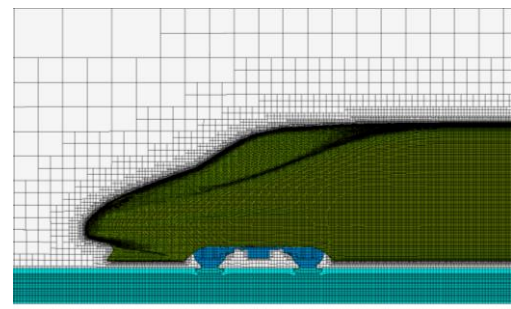
(b)

Fig. 4. Computational mesh: (a) Global mesh and (b) Boundary layers around the train body.

Table 1 Results for different mesh resolutions

Grid	Number of Cells	C_D	C_L	C_C
Coarse	12 millions	0.137	0.465	0.782
Baseline	24 millions	0.161	0.502	0.843
Fine	96 millions	0.165	0.513	0.865

In this paper, uniform wind speeds of 83.33 m/s, 83.67 m/s, 84.67 m/s, 86.32 m/s and 88.53 m/s are separately given at the inlet, considering the same train speed at different yaw angles, seeing Fig. 3(a). A static pressure of 0 is given at the outlet. The up-wall and side-walls of the computational domain are set as no-slip stationary walls. The STBR scenario and ground are set as no-slip moving walls with the velocity of 83.33 m/s in the opposite direction of the F_x direction, as shown in Fig. 3(a). The train and bogie surfaces are treated as no-slip stationary walls. In this paper, the commercial CFD software solver ANSYS FLUENT was used. The numerical simulation calculation was based on a pressure solver, and the SIMPLEC algorithm was used to couple the pressure and velocity fields. The Finite Volume Method (FVM) based on central difference

was chosen to discrete the governing equations, and a second-order upwind scheme was selected to solve the k and ε equations. The solution was considered converged when the residuals were smaller than the recommendation of 10^{-3} in Fluent and the fluctuation in drag force, lift force, lateral force and overturning moment were within 1% of the total values.

2.4 Emission Plane of Sand Particles and DPM Details

Limited by computing resource, the quantity and distribution of sand particles should be reduced to the minimum necessary, thus, the emission plane area and the injection number must be reasonable. The aim of this paper is to study the influence of sand collision on the head car, so the sand particles have been released in a vertical emission plane which is larger than the projected area of the train on the cross-section of the domain. Figure 5 presents the position and size of the emission plane in the computational domain. The plane locates at 7*H* away from the inlet with the height of 1.5*H*. The width of the emission plane should be longer than the maximal lateral projected distance of the head car subjected to the yaw angle of 19.73 degrees. So the width of the plane is *W*=5.5*H*, and 3.5*H* far away from the upper side-wall, as shown in Fig. 5. Owing to a large number of volume meshes around the vehicle, the emission plane contains lots of injection particles, resulting in a need of numerous computations. To rationally make use of computing resources, the ANSYS FLUENT's User Defined Functions (UDFs) have been adopted to limit the quantities of injected particles following an equally spatial distribution in the emission plane so as to improve the efficiency of the numerical simulation.
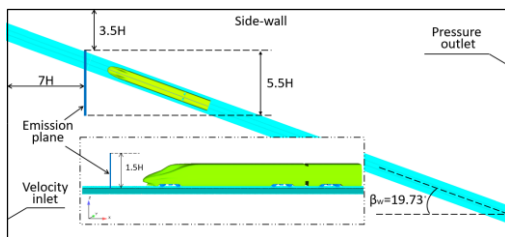

Fig. 5. Dimensions of the emission plane.

In the DPM model, the diameter, restitution coefficient and volume fraction of the sand particles can have great effects on the numerical results. So in this study, the worst case (strong sandstorms) was taken into account, i.e. the volume fraction of the sand particles is 1.08e According to the International Scale for the identification and classification of soils ISO 14688-1 (ISO 2002), the diameter of the medium and fine sand particles varies from 0.1 to 0.5mm. Thus, the diameter of 0.1, 0.3, and 0.5mm were chosen in the simulation. The Stokes number, S_{tk}, describing the following characteristics of particles can be calculated in the formula (8), and the Stokes number ranges from 1.842 to 48.923.

$$S_{tk} = \frac{\rho_p d_p^2 u}{18 \mu H} \tag{8}$$

In addition, the restitution coefficient of sand particles will also affect the aerodynamic performance evidently. The restitution coefficient can be defined as the ratio between the velocity normal to the surface before and after the impact, namely, the restitution coefficient is the ratio of U_{p1} and U_{p2}, as shown in Fig. 6. The restitution coefficient of 0.6, 0.8 and 1.0 were adopted to investigate the effect of restitution coefficients of sand collision on aerodynamic performance of high-speed train in sandstorms in the present study, according to previous study published by Paz *et al.* (2015). The train surfaces are set as the reflect condition with the restitution coefficient of 0.6, 0.8 and 1.0. The boundary surfaces of the computational domain and the STBR scenario were set as escape conditions. A two-way coupling method between the continuous phase and discrete phase was selected. In order to guarantee the trajectory of the sand particles can pass through the whole computational domain, the iteration time was 3s, and the particle time step size was 0.001s.

The aerodynamic loads caused by sand collision are calculated by averaging the change of particles' momentum over the time between two consecutive impacts. For each sand particle, this time is defined as $\Delta t_i = \Delta l_i / |U_{pi1}|$, where Δl_i is the distance between successive particles and $|U_{pi1}|$ is the velocity of the *i*th particle, as shown in Fig. 6. The mean force exerting on the train caused by the sand collision can be calculated by Eq. (9)

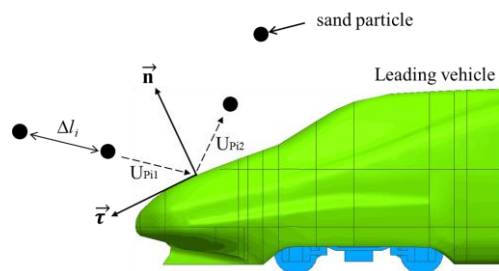$$F_{mean} = \sum_i \left[\frac{m_p (U_{pi2} - U_{pi1})}{\Delta t_i} \right] \tag{9}$$

Fig. 6. Sketch of the impact of sand particles on the surface of the head car.

3. RESULTS AND DISCUSSION

3.1 Validation

In order to validate the simulation correctness of the continuous phase, the test was conducted in the second test section of $8m \times 6m$ wind tunnel in the China Aerodynamics Research and Development Center (CARDC). To reduce the thickness of the approaching boundary layer, a fixed ground board with a rotating table device was installed, as shown in Fig. 7. The distance of the floor device to the lower wall of the wind tunnel is 1.06m. The size of

test section is $4.94\text{m} \times 8\text{m}$, and the cross-sectional area of the train model with the scale of 1:8 is 0.175m^2. Therefore, the blockage ratio is much less than 5%, which means the experimental results do not need to be corrected.
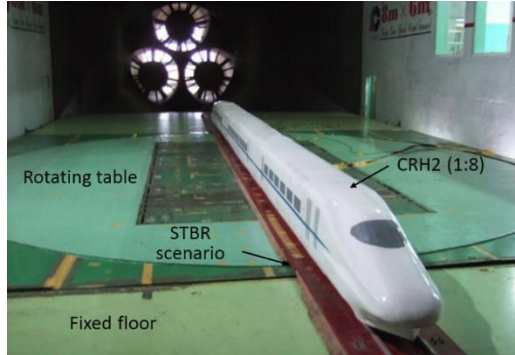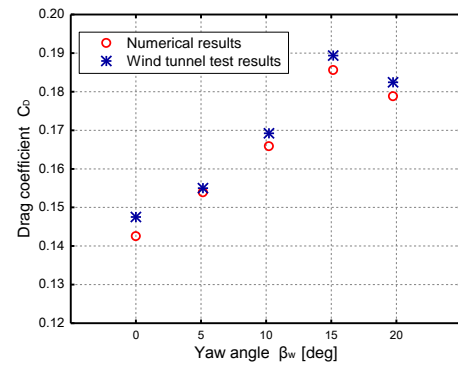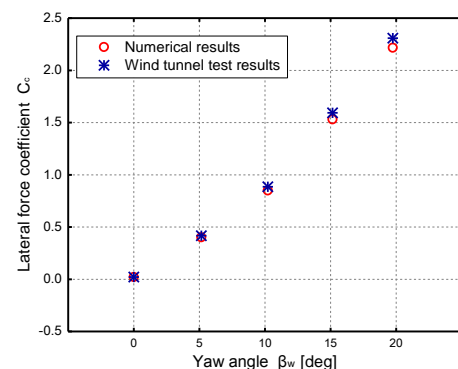

Fig. 7. Wind tunnel test setup.

The geometry model and computational domain were the same as the experimental setup. The 1/8th scaled CRH2 train model grouped as three cars (the head car, the middle car and the tail car) was adopted. The resolution of the mesh and methodology mentioned in Section 2 were also adopted in this section.

(a)

(b)

Fig. 8. Comparison between the numerical results and wind tunnel test results: (a) drag coefficient and (b) lateral force coefficient.

As shown in Fig. 8, the drag force coefficients and the lateral force coefficients at different yaw angles

in the numerical simulations are close to the results in the wind tunnel tests, and the maximum error of the drag and the lateral force coefficients between the numerical and experimental results are 6.8% and 3.8%, respectively. Therefore, the resolution of the mesh and methodology is sufficient to achieve a high accurate prediction in the continuous phase. Unfortunately, no reference data are available in the field of sand particle impacts in aerodynamic performance of high-speed trains under crosswind condition to validate this two discrete phase method. The existing studies exploring the effect on airfoils caused by heavy rain (Valentine and Decker 1995) or the influence of dust on the solar thermal collectors (García 2014), are not suitable for comparison with this work.

3.2 Impact of Sand Particle Diameters and Restitution Coefficients on the Aerodynamic Coefficients

Figure 9 presents the influence of sand particles' properties (diameter and restitution coefficient) on the train aerodynamic performance. The values of aerodynamic coefficients, such as the drag force coefficient, lift force coefficient, lateral force coefficient and overturning moment coefficient are given by a ratio between the aerodynamic coefficients generated by the sand particles and the overall aerodynamic coefficients of the head car. All the aerodynamic coefficients ratios in Fig. 9(a) are positive, illustrating the aerodynamic coefficients of high-speed trains in strong sandstorms increase as compared to the no-sand condition. The sand particles' properties have great effects on the drag force coefficient ratio due to the sand. The increasing diameter of sand particles lead to more contribution to the drag force coefficient, for example, at the yaw angle of 0 degree, for the restitution coefficient of 1.0, the drag force coefficient ratio grows from 3.74% (sand particle diameter of 0.1mm), to 6.91% (0.3mm) and 10.38% (0.5mm). As it is known in the formula (7), the Stokes number is proportional to the square of the sand particle's diameter. The sand particle with a higher Stokes number that shows a weak following characteristic has more possibility to separate with the streamlines and directly impact on the surface of the head car (Paz *et al.* 2015). Furthermore, the restitution coefficient also affects the drag force coefficient ratio a lot. At the yaw angle of 0 degree, for the sand diameter of 0.5mm, compared to the drag contribution at the restitution coefficient of 0.6, it rises by 16.44% when the restitution coefficient is 0.8 and 29.12% (restitution coefficient of 1.0). Because of the impact between the sand particles and the head car with higher restitution coefficients, the momentum changes of the sand particles increase, accordingly, the force acting on the vehicle caused by sand collision increases a lot, according to the momentum law. Figure 9(a) also shows the dominant effect on the drag force ratio is the sand diameter compared to the restitution coefficient. At the yaw angle of 19.73 degrees, an increase of 0.2mm of the diameter leads to the increase of about 6% of drag force ratio, while the 0.2 increase of the restitution coefficient leads to approximate 2% increase of the drag force ratio.
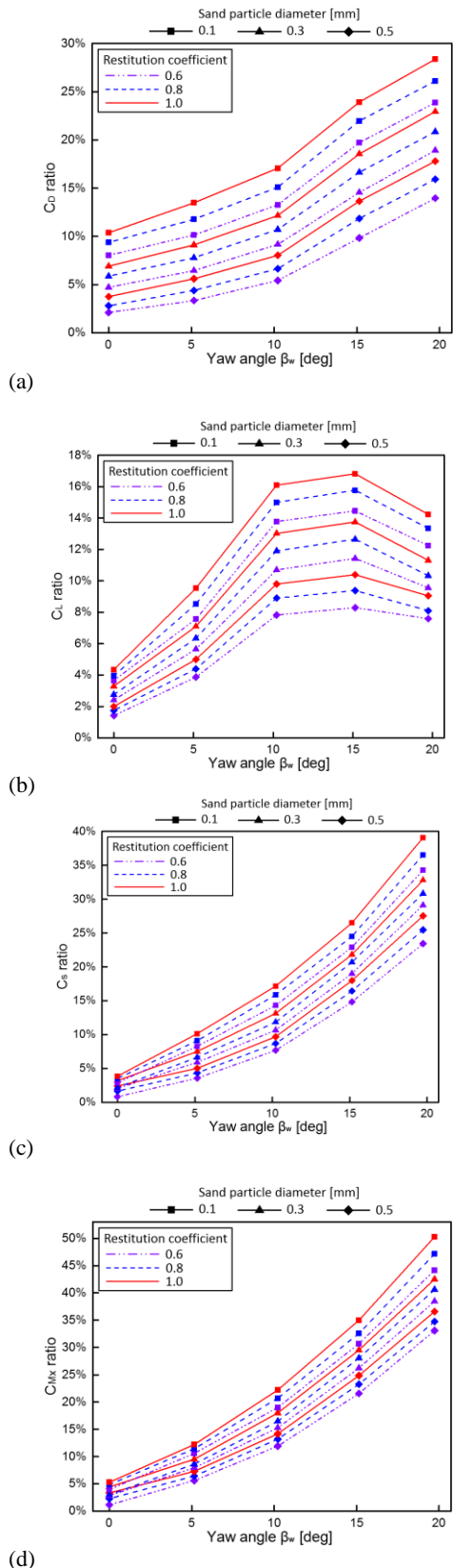
(a)

(b)

(c)

(d)

Fig. 9. Graphs of the aerodynamic coefficients: (a) drag force coefficient, (b) lift force coefficient, (c) lateral force coefficient and (d) overturning moment coefficient ratio of the head car as a function of yaw angles for different values of the sand particle's diameter and coefficient of restitution.

Figure 10 presents the numerical results of streamlines at different yaw angles. The streamlines rise up at the windward surface of the head car and flow over the roof of the vehicle, and then separation occurs at the leeward of the vehicle (Cheli *et al.* 2010). The sand particles following the streamlines moves towards the windward surface of head car, then they separate with the rising streamlines and impact on the head car at an upward velocity component due to the inertia, which increases the lift force coefficient of the head car. Figure 9(b) shows that the lift force increases with the particle diameter increasing, due to the increasing possibility of the sand impact on the vehicle. For instance, at the yaw angle of 15.14 degrees, for the restitution coefficient of 1.0, the lift force coefficient ratio grows from 10.38% (sand particle diameter 0.1mm), to 13.75% (0.3mm) and 16.10% (0.5mm). The presence that the lift force ratio increases with the increasing restitution coefficient is the result of the larger upward force of the vehicle due to the impact of sand particles. The lateral force coefficient ratio and overturning moment coefficient ratio in Figs. 9(c) and 9(d) are both positive, indicating that the sand collisions play an inferior role on the lateral aerodynamic performance of the head car, which has a potential of posing a safety threat on the high-speed trains running in the sandstorms weather. The sand property also plays a significant role in the lateral force and overturning moment coefficient ratio. For the restitution coefficient of 1.0 and yaw angle of 19.73 degrees, compared to the lateral force and overturning moment coefficient ratio at the restitution coefficient of 0.6, the contribution to lateral force and overturning moment rise by 19.14% and 16.12% (sand particle's diameter of 0.3mm), 41.92% and 37.38% (0.5mm). The incremental restitution coefficient also leads the higher ratio of the lateral force and overturning moment. As a result, it limits the critical running speed of the high-speed trains and lowers the transportation efficiency (Xiong *et al.* 2011).

3.3 Influence of Yaw Angles on the Sand Particles' Contribution to the Aerodynamic Coefficients

As it can be seen from Fig. 9, the aerodynamic coefficient ratios change with yaw angles. Figure 9(a) shows that the drag force ratio increases with the yaw angles increasing. This phenomenon can be explained that on the one hand the increasing yaw angles raise the effective sand collision area and the quantity of sand particles impacting on the vehicle; on the other hand, the velocities of the streamlines flowing towards the windward surface of the head car become higher at a larger yaw angles, which results in a larger Stokes number of the sand particles according to the formula (8) and increases the impact probability. The component of sand particles' momentum impacting on the vehicle is opposite to the high-speed train's running direction. The change rates of the drag force coefficient ratio first increase then decrease with the increase of yaw angles. When the yaw angle is less than 15.14 degrees, the change rates increase with the yaw
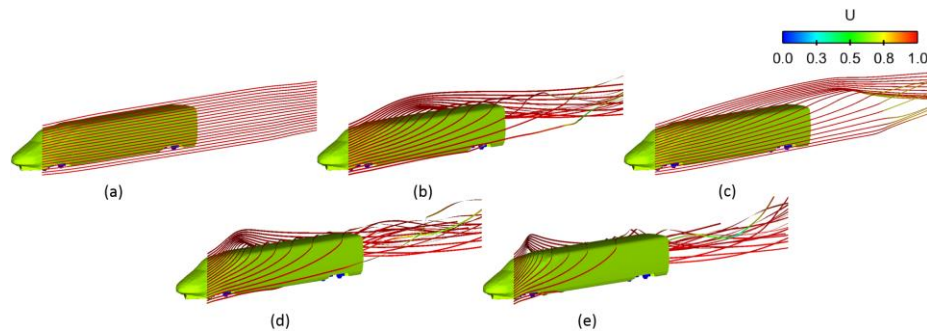
Fig. 10. 3D **streamlines analysis around the head car at different yaw angle: (a) 0°, (b) 5.15°, (c) 10.22°, (d) 15.14° and (e) 19.73°.**

angle increasing, and then decrease as the yaw angle excesses 15.14 degrees. Figure 9(a) also shows that the difference of the drag force coefficient ratio between different sand particle diameters at different yaw angles, when the restitution coefficient is constant. At a certain particle diameter, the influence of the restitution coefficient on the drag force ratio becomes larger. The yaw angles enhance the effects of sand properties (diameter and restitution coefficient) on the drag force coefficients of the head car.
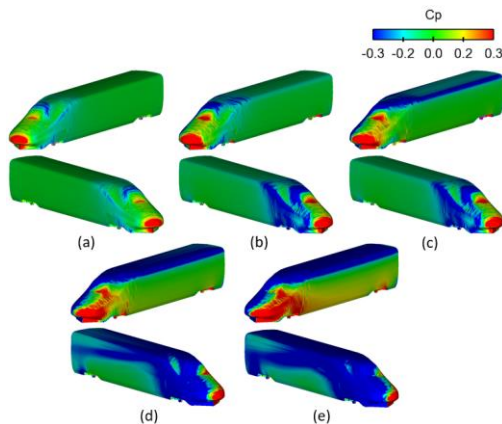

Fig. 11. Pressure distributions on the windward and leeward sides of the head car at different yaw angles: (a) 0°, (b) 5.15°, (c) 10.22°, (d) 15.14° and (e) 19.73°.

The absolute value of the negative pressure on the vehicle's roof increases with the yaw angle increasing, as shown in Fig. 11, and changes faster than on the bottom of the vehicle (Flynn *et al.* 2016), which results in larger lift force coefficients. The sand properties have little effect on the lift force coefficients with no yaw angle. Within the range from 0 to 10.22 degrees, the impact probability raises with the yaw angle increasing, which stimulates the contribution to the lift force due to the sand. Then the contribution to the lift force caused by sand impact and sand properties tends to be stable. As the yaw angle excesses15.14 degrees, the pressure difference between the roof and bottom of the vehicle increase, which inhibits the influence of sand properties on the lift force coefficient ratio.

Figure 11 shows that the pressure distributions on the windward and leeward sides of the head car at different yaw angles. The positive pressure area moves to the transition between the streamlined head and vehicle body from the nose of the head car, which is similar to the regularity reported in Tomasini (2014). Because of the coupling effect of strong crosswind and train wind, the side force coefficients increase with the yaw angles increasing. At the yaw angle of 0 degree, the sand particles perform little effect on the side force coefficients, because the sand particles are more likely to follow the streamlines, Fig. 10(a), flowing parallel to the vehicle length rather than impacting on the vehicle sides. However, as the yaw angles continues to increase, the sand collision plays a more significant role in the side force coefficients due to the increase of the quantities of the sand particles impacting on the windward surface of the vehicle. The effects of sand properties (diameter and restitution coefficient) on the side force are also strengthened at a larger yaw angle because of the increasing impact possibility and effective impact area.

As shown in Fig. 9(d), the overturning moment coefficient ratio is less than 5% at the yaw angle of 0. As the yaw angle increases, the contribution to the overturning moment increase largely, and the change rate of overturning moment coefficient ratio also increases gradually. At the yaw angle of 19.73 degrees, the overturning moment ratio achieves the maximum of 50.28%. Figure 9(d) shows that the trends of overturning moment ratios changing with yaw angles, which are approximate in line with the trends of lateral force ratios in Fig. 9(c). So the overturning moment mainly comes from the lateral force, which shows good agreement with the regularity reported in Giappino (2016). Figure 9(d) clearly illustrates that the yaw angle enhance the effect of sand properties on the overturning moment coefficient ratio. And it also should be noted that the influence of sand diameters on the overturning moment ratio increases at a larger restitution coefficient. Similarly, the effects on the overturning moments caused by the restitution coefficients enhance with the increase in the diameter of sand particles. Therefore, the particle diameter and restitution coefficient strengthen the effect each other on the contribution to the overturning moment coefficient ratio.

3.4 Coating Effect of Energy Conservation and Running Safety of High-Speed Trains

The restitution coefficient of sand particles are mainly determined by the coating material around high-speed trains, so the use of appropriate coatings have great effects on the aerodynamic performance of the high-speed trains running in sandstorm weather. As shown in Fig. 9(a), the coatings of high-speed trains are so important because a decrease of 0.2 in the restitution coefficient indicates that about 6% drag reduction when the train is subjected to the yaw angle of 19.73 degrees and the sand particle with the diameter of 0.5mm. Considered the operational time and frequency of the high-speed train in such wind-sand environments, e.g. the Lanchow-Xinjiang railway in China, 6% represents a substantial sum of energy can be saved. In Fig. 9 (b), the lift force coefficient ratios reduce by about 4% with the decrease of 0.2 of the restitution coefficient of the sand particles with the diameter of 0.5mm at the yaw angle of 15.14 degrees. Figs. 9(c) and 9(d) present that a 0.2 decrease in the restitution coefficient indicates an about 6% reduction in the lateral force coefficient ratio and about 8% reduction in the overturning moment ratio when the diameter of sand particles is 0.5mm and the yaw angle is 19.73 degrees. As described in CEN European Standard (CEN European Standard 2013), the simplest approach to calculate the critical speed of high-speed trains needs a three-mass model. It is can be obtained that the lower overturning moment coefficient of high-speed trains corresponds to the higher critical train speed (Giappino 2016). Therefore, the use of coatings can not only enhance the operational stability and safety of the high-speed trains under strong sandstorm conditions, but also improve the speed limit and transportation efficiency.

4. CONCLUSIONS

In this study, the aerodynamic performance of the head car of a CRH2 train running in sandstorms with yaw angles was investigated using a DPM model. The effects of sand collision on the aerodynamic performance of the head vehicle was analysed. The numerical results of flow fields around the high-speed train were validated against experimental results. Based on these results, the following conclusions can be drawn.

(1) The diameter of sand particles is found to have great effects on the aerodynamic loads due to sand collision. A 0.2 mm increase in the sand diameter can cause an increase by approximate 50% of the contribution to the drag of the head vehicle without yaw. A larger diameter allows more sand particles to separate with the streamlines and directly impact on the surface of the head car.

(2) With the increase of the yaw angle, the impact chance between the sand particles and the vehicle surface also increases, causing more contribution to aerodynamic performance of high-speed trains. A larger yaw angle gives a more significant impact of the particles' properties on the drag force, lateral force and overturning moment coefficient ratios. However, the effect of sand properties on the lift force coefficient ratio is reduced once the yaw angle excesses 15.14 degrees.

(3) For the improvement of aerodynamic performance of high-speed trains running in sandstorms, the use of appropriate coatings around the surfaces of the high-speed trains to decrease the restitution coefficient of sand particles is recommended. For a decrease of 0.2 in the restitution, an approximate 6% drag reduction at the yaw angle of 0 degree and 8% reduction of the overturning moment can be achieved, which not only significantly decrease the operational costs, but also greatly improve the crosswind stability and critical running speed of the train in the sandstorms.

REFERENCES

Baker, C. J. (1991a). Ground vehicles in high cross winds part 1: steady aerodynamic forces. *Journal of Fluids & Structures* 5(1), 69–90.

Baker, C. J. (1991b). Ground vehicles in high cross winds part II: Unsteady aerodynamic forces. *Journal of Fluids & Structures* 5(1), 91–111.

Balachandar, S. and K. John (2010). Turbulent Dispersed Multiphase Flow [J]. *Fluid Mechanics* 42(42), 111-133.

Barisam, M., M. Shams (2015). A three-dimensional two phase method for predicting drug delivery to tumor. *Powder Technology* 283, 530-538.

Bocciolone, M., F. Cheli and R. Corradi (2008). Crosswind action on rail vehicles: Wind tunnel experimental analyses. *Journal of Wind Engineering & Industrial Aerodynamics* 96(5), 584-610.

CEN European Standard 2013. Railway applications aerodynamics Part 6: Requirements and test procedures for crosswind assessment. CEN EN, 14067-14074.

Cheli, F., F. Ripamonti and D. Rocchi (2010). Aerodynamic behaviour investigation of the new EMUV250 train to cross wind. *Journal of Wind Engineering & Industrial Aerodynamics* 98(4), 189-201.

Cheli, F., G. Diana and F. Ripamonti (2006). Aerodynamic Sensitivity Analysis of the New EMUV250 Train to Cross Wind By Wind Tunnel Test And CFD Analysis. *European Conference on Computational Mechanics*. Springer Netherlands, 766-766.

Cheli, F., S. Giappino and L. Rosa (2013). Experimental study on the aerodynamic forces on railway vehicles in presence of turbulence. *Journal of Wind Engineering & Industrial Aerodynamics* 123(6), 311-316.

Diedrichs, B. (2003). On computational fluid dynamics modelling of crosswind effects for high-speed rolling stock. *Proceedings of the Institution of Mechanical Engineers Part F Journal of Rail & Rapid Transit* 217, 203-226.

Dorigatti, F., M. Sterling and C. J. Baker (2015). Crosswind effects on the stability of a model passenger train-A comparison of static and moving experiments. *Journal of Wind Engineering & Industrial Aerodynamics* 138, 36-51.

Flynn, D., H. Hemida and C. Baker (2016). On the effect of crosswinds on the slipstream of a freight train and associated effects. *Journal of Wind Engineering & Industrial Aerodynamics* 156, 14-28.

García, E. T. (2014). On the effects of windbreaks on the aerodynamic loads over parabolic solar troughs. *Applied Energy* 115(4), 293-300.

Giappino, S., D. Rocchi and P. Schito (2016). Cross wind and rollover risk on lightweight railway vehicles. *Journal of Wind Engineering & Industrial Aerodynamics* 153, 106-112.

Gilbert, T., C. J. Baker and A. Quinn (2013). Gusts caused by high-speed trains in confined spaces and tunnels. *Journal of Wind Engineering & Industrial Aerodynamics* 121, 39–48.

Guan, H. Y. and J. Y. Tu (2010). Computational Techniques for Multi-phase Flows. *Amsterdam Elservier.*

Hemida, H., C. Baker and G. J. Gao (2014). The calculation of train slipstreams using large-eddy simulation. *Proceedings of the Institution of Mechanical Engineers Part F Journal of Rail & Rapid Transit* 228(1), 25-36.

Hemida, H. and S. Krajnović (2010). LES study of the influence of the nose shape and yaw angles on flow structures around trains. *Journal of Wind Engineering & Industrial Aerodynamics* 98(1), 34-46.

ISO 2002. Geotechnical investigation and testing–Identification and classification of soil Part1: Identification and description. 14688-1.

John, D. and J. R. Anderson (1995). Computational fluid Dynamics: The Basics with Applications. *McGraw-Hill series in mechanical engineering.*

Morsi, S. A. and A. J. Alexander (1972). An Investigation of Particle Trajectories in Two-Phase Systems. *Journal of Fluid Mechanics* 55(2), 193- 208.

Ni, J. R. and Z. S. Li (2006). Wind blowing sand two-phase flow theory and its application. *Beijing: Science Press.*

Nieto, P. J. G. (2010). Numerical simulation of the performance of a snow fence with airfoil snow plates by FVM. *Journal of Computational & Applied Mathematics* 234(4), 1200-1210.

Orellano, A. (2009). Cross-wind effects on road and rail vehicles. *Vehicle System Dynamics* 47(8), 983-1022.

Paz, C., E. Suárez and C. Gil (2015). Numerical study of the impact of windblown sand particles on a high-speed train. *Journal of Wind Engineering & Industrial Aerodynamics* 145(1), 87-93.

Safikhani, H. and P. Mehrabian (2016). Numerical study of flow field in new cyclone separators. *Advanced Powder Technology* 27(2), 379-387.

Shih, T. H., W. W. Liou and A. Shabbir (1995). A new k-epsilon eddy viscosity model for high reynolds number turbulent flows. *Computers & Fluids* 24(3), 227-238.

Spalding, D. B. (1981). Numerical computation of multi-phase flows. *Von Karman Inst for Fluid Dyn Numerical Computation of Multi-Phase Flows.*

Tomasini, G., S. Giappino, R. Corradi (2014). Experimental investigation of the effects of embankment scenario on railway vehicle aerodynamic coefficients. *Journal of Wind Engineering & Industrial Aerodynamics* 131, 59-71.

Valentine, J. R. and R. A. Decker (1995). A Lagrangian-Eulerian scheme for flow around an airfoil in rain. *International Journal of Multiphase Flow* 21(4), 639-648.

Xiong, H. B., W. G. Yu and D. W. Chen (2011). Numerical study on the aerodynamic performance and safe running of high-speed trains in sandstorms. *Journal of Zhejiang University-SCIENCE A* 12(12), 971-978.

Zhang, J., G. J. Gao, T. H. Liu and Z. W. Li (2015). Crosswind stability of high-speed trains in special cuts. *Journal of Central South University* 22(7), 2849-2856.

Zhang, J., K. He, X. H. Xiong, J. B. Wang and G. J. Gao (2017) Numerical Simulation with a DES Approach for a High-Speed Train Subjected to the Crosswind. *Journal of Applied Fluid Mechanics* 10(5), 1329-1342.

Zhang, Z. and Q. Chen (2007). Comparison of the Eulerian and Lagrangian methods for predicting particle transport in enclosed spaces. *Atmospheric Environment* 41(25), 5236-5248.

Zhu, J., Z. Hu and D. J. Thompson (2015). Flow behaviour and aeroacoustic characteristics of a simplified high-speed train bogie. *Proceedings of the Institution of Mechanical Engineers Part F Journal of Rail & Rapid Transit*. Available online.